This manuscript was accepted by J. Appl. Phys. Click here to see the version of record.

Thermoelectric transport of GaAs, InP, and PbTe: Hybrid functional with $\boldsymbol{k}\cdot\tilde{\boldsymbol{p}}$ interpolation versus scissor-corrected generalized gradient approximation

Kristian Berland[1,*] and Clas Persson[1]

[1] *Centre for Materials Science and Nanotechnology, Department of Physics, University of Oslo, Norway*

Boltzmann transport calculations based on band structures generated with density functional theory (DFT) are often used in the discovery and analysis of thermoelectric materials. In standard implementations, such calculations require dense $\boldsymbol{k}$-point sampling of the Brillouin zone and are therefore typically limited to the generalized gradient approximation (GGA), whereas more accurate methods such as hybrid functionals would have been preferable. GGA variants, however, generally underestimate the band gap. While a premature onset of minority carriers can be avoided with scissor corrections, the band gap also affects the band curvature. In this study, we resolved the $\boldsymbol{k}$-point sampling issue in hybrid-functional based calculations by extending our recently developed $\boldsymbol{k}\cdot\tilde{\boldsymbol{p}}$ interpolation scheme [Comput. Mater. Sci. 134, 17 (2017)] to non-local one-electron potentials and spin-orbit coupling. The Seebeck coefficient generated based on hybrid functionals were found to agree better than GGA with experimental data for GaAs, InP, and PbTe. For PbTe, even the choice of hybrid functional has bearing on the interpretation of experimental data, which we attribute to the description of valley convergence of the valence band.

I. INTRODUCTION

By converting heat to electricity, thermoelectrics can recover some of the immense waste heat generated in transport, power generation, and industrial processes. The aim of reducing global CO_2 emissions and recent record thermoelectric conversion efficiencies[1] have led to renewed interest in optimizing and uncovering new thermoelectric materials. Such efforts are aided by the Boltzmann transport equation (BTE) based calculations based on first-principles density functional theory (DFT). For instance, the doping concentration that maximizes the product of electrical conductivity σ and the Seebeck coefficient squared S^2, i.e. the thermoelectric power factor σS^2, can be easily estimated by shifting the Fermi level μ_{F} in the calculations. A large power factor and low thermal conductivity κ is essential for obtaining a large figure of merit $ZT = \sigma S^2 T/\kappa$. With DFT-generated band structure, non-parabolicity and multi-valley are included from the onset, which is key in computational screening of thermoelectric materials.[2–7] However, such calculations are limited by the need for dense sampling of the Brillouin zone.[8] This is not a major issue when employing semi-local exchange-correlation (XC) functionals in the generalized gradient approximation (GGA),[9] but more sophisticated approaches such as hybrid functionals[10,11] and GW[12,13] are typically out of reach.

Many thermoelectric materials including PbTe have narrow direct band gaps, which leads to large non-parabolicity and small effective masses – in a two-band Kane model, the effective mass is given by $m = (3\hbar^2/4P^2)E_{\mathrm{gap}}$, where P is the momentum matrix coupling between the two bands.[14] Thermoelectric power factors can, therefore, be optimized by effectively tuning the band gap using solid solutions, strain, or native vacancies.[15] While scissor corrections can be used to avoid premature onsets of minority carrier transport caused by GGA's underestimated band gaps,[16,17] this approach does not correct effective masses and non-parabolicity.[18,19] Unlike for dielectric functions,[20,21] there is no formal justification for using scissor corrections for transport properties. While underestimated gaps can be avoided with certain GGAs,[22,23] meta-GGAs,[24] and related schemes[25,26] designed to improve band gaps at low computational costs, more computationally demanding methods, such as hybrid functionals and GW, can be desirable for describing broad classes of solids. The same hybrid functional can also be employed for optimizing the structure as for computing the band structure. Moreover, perturbative methods, generally do not correct inaccurate electronic densities which could arise for materials incorrectly found to be semimetals and could fail to resolve spurious band hybridizations. For transport calculations, the more computationally demanding methods can be employed if the band structure is accurately interpolated. In particular, interpolation methods that make use of information in the Kohn-Sham (KS) wave functions, such as the Shirley,[27,28] or the Wannier[29–32] method can be efficient. Recently, we developed the $\boldsymbol{k}\cdot\tilde{\boldsymbol{p}}$ method,[33] which corrects the standard extrapolative $\boldsymbol{k}\cdot\boldsymbol{p}$ method[34] by ensuring that the $\boldsymbol{k}\cdot\boldsymbol{p}$ and KS energies match on a coarse mesh. In this work, we extended the scheme to hybrid functionals and spin-orbit coupling by replacing momentum-matrix elements by velocity-matrix elements.

Beyond the effect of direct band gaps, an accurate band structure is also important when using computational methods to optimize thermoelectric properties, such as in identifying suitable impurities with energy levels resonating with conduction or valence bands,[35] or when determining the solid solution composition or strain that optimally aligns band extrema of multiple degenerate band valleys.[15] Such valley convergence increases the number of conductive channels which enhances σ without reducing S and has been employed to optimize thermoelectric transport properties of $Mg_2Si_{1-x}Sn_x$[36] and $PbTe_{1-x}Se_x$.[37] Approximate valley convergence is itself

one of the reasons why PbTe exhibits a high power factor.[37]

The next section illustrates the need for a dense $\boldsymbol{k}$-mesh in BTE calculations using BoltzTraP[8] and the effectiveness of our interpolation method. In Sec. III, the thermoelectric transport properties of hybrid functionals and scissor-corrected GGA are compared for the direct band-gap III-V semiconductors GaAs, InP and the cubic chalcogenide PbTe. While III-V semiconductors are not traditional thermoelectric materials, they are important in electronics. Here they serve as model systems as GGA significantly underestimates their band gap energies and accurate experimental Seebeck coefficient are available for a range of doping concentrations. PbTe, on the other hand, is a narrow-gap thermoelectric material of significant scientific and commercial interest. In the final section, we offer our perspective on prospects of enhancing the accuracy and predictability of first-principles calculations of thermoelectric properties.

II. METHOD

A. Density functional theory calculations

The atomic and electronic structure were obtained using DFT with the projector-augmented plane wave code VASP.[38–41] Three different functionals were considered for obtaining the electronic structure: the GGA functional PBE,[9] the screened hybrid HSE06[11] (hereafter HSE) and the hybrid PBE0.[10] These calculations relied on a $12 \times 12 \times 12$ $\boldsymbol{k}$-point sampling of the Brillouin zone and 64 bands in total with spin-orbit coupling included.

For each of these three functionals, the atomic structure was kept the same to solely explore the effect of the XC functional on the band structure and exclude effects arising from differing lattice parameters. The atomic structures[72] employed were relaxed using the GGA functional PBEsol[42] with a $10\times10\times10$ $\boldsymbol{k}$-point sampling and an energy cutoff set 30% above the standard high energy cutoff. We employ PBEsol as it generally provides a more accurate lattice constants of solids than PBE.[43] However, we note that a proper comparison of the accuracy of the different functionals would require taking thermal expansion into account, as this affects the effective mass[44] and non-parabolicity of the compounds. However, such a calculation is beyond the scope of this paper.

B. Corrected $\boldsymbol{k}\cdot\boldsymbol{p}$-based interpolation scheme

Developed in the 1950s, the $\boldsymbol{k}\cdot\boldsymbol{p}$ method[45–47] has become a standard method to represent electronic band structures. It has found wide usage in the envelope-function formalism,[48–50] which extends the theory to semiconductor heterostructures. The $\boldsymbol{k}\cdot\boldsymbol{p}$ Hamiltonian at a given $\boldsymbol{k}$ is given in terms of Bloch wave function basis of a specific $\boldsymbol{k}_0$, i.e. $\psi_{i,\boldsymbol{k}_0}(\boldsymbol{r}) = u_{i,\boldsymbol{k}_0}(\boldsymbol{r})e^{\mathrm{i}\boldsymbol{k}_0\cdot\boldsymbol{r}}$. The

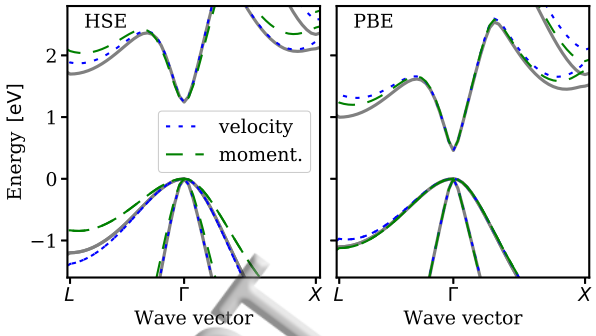

FIG. 1: Calculated band structure of GaAs. The panels compare the KS result generated with HSE (left panel) and PBE (right panel) with the 15-band $\boldsymbol{k}\cdot\boldsymbol{p}$ result, with momentum- (green, long-dashed) and velocity- (blue short-dashes) matrix elements calculated at the Γ-point.

Hamiltonian is given by

$$H_{ij}(\boldsymbol{k}) = \left(\varepsilon_{i,\boldsymbol{k}_0} + \frac{\hbar^2\left(\boldsymbol{k}-\boldsymbol{k}_0\right)^2}{2m}\right)\delta_{ij} + \frac{\hbar(\boldsymbol{k}-\boldsymbol{k}_0)\cdot\boldsymbol{p}_{ij}}{m}, \tag{1}$$

where $\varepsilon_{i,\boldsymbol{k}_0}$ are the electron eigenvalues at $\boldsymbol{k}_0$ and $\boldsymbol{p}_{ij} = \langle\psi_{i,\boldsymbol{k}_0}|\hat{\boldsymbol{p}}|\psi_{j,\boldsymbol{k}_0}\rangle$ are the corresponding momentum matrix elements and m is the free-electron mass. Traditionally, the $\boldsymbol{k}\cdot\boldsymbol{p}$ Hamiltonian is parameterized, for a finite number of bands, based on a combination of measured and calculated properties,[51–54] leading to, for instance, two-, eight- and thirty- band models etc.[54] Here we avoid this empiricism by computing the matrix elements directly using DFT.

The $\boldsymbol{k}\cdot\boldsymbol{p}$ Hamiltonian is an exact representation of the Schrödinger equation for local potentials, $V(\boldsymbol{r})$, in the limit of an infinite number of bands. However, practical calculations are based on a finite number of bands and plane-wave DFT calculations often rely on non-local pseudopotentials, both contribute to making the $\boldsymbol{k}\cdot\boldsymbol{p}$ Hamiltonian inexact. In our previous work,[33] we employed the harder so-called "GW" projector-augmented wave (PAW) pseudopotentials to enhance the accuracy of the $\boldsymbol{p}_{ij}$ matrix elements.[38–40] Truly local potentials can be obtained with all-electron codes or exact PAW calculations. However, for hybrid functionals, the Fock exchange part is intrinsically non-local. To extend the $\boldsymbol{k}\cdot\boldsymbol{p}$ method, and hence our interpolation scheme, to non-local potentials, we replaced the momentum matrix elements $\boldsymbol{p}_{ij}$ by velocity (i.e. conjugate momentum) matrix elements $m\boldsymbol{v}_{ij} = \frac{\mathrm{i}}{\hbar}\langle\psi_{i,\boldsymbol{k}_0}|[H,\boldsymbol{r}]|\psi_{j,\boldsymbol{k}_0}\rangle$. This choice makes the $\boldsymbol{k}\cdot\boldsymbol{p}$ Hamiltonian (1) exact to second order in $(\boldsymbol{k}-\boldsymbol{k}_0)$.[55] Moreover, these matrix elements include spin-orbit coupling if this was employed at the DFT level. The velocity matrix elements were obtained by adapting VASP[38–40] routines for calculating dielectric function in the longitudinal gauge.[41] With velocity, rather than momentum matrix elements, we found no appreciable advantage in using the harder "GW pseudopotentials", and

This manuscript was accepted by J. Appl. Phys. Click here to see the version of record.

we, therefore, employed standard PAW pseudopotentials in this work.

Figure 1 compares the HSE (left panel) and PBE (right panel) band structure of GaAs with the $\boldsymbol{k}\cdot\boldsymbol{p}$ band structure generated with 15 bands using respectively momentum (long dashes) and velocity matrix elements (short dashes). Spin-orbit coupling is not included in the comparison as we were only able to extract it with velocity-matrix elements. The figure shows that for HSE, velocity matrix elements provide far better agreement with the KS band structure than momentum matrix elements. For PBE, both agree well with the KS band structure, with momentum matrix elements providing a slightly better agreement, which could in part be due to error cancellations, such as the use of a finite number of bands.

Depending on the solid, we found that the Γ-point based $\boldsymbol{k}\cdot\boldsymbol{p}$ method does not generally agree as well with the KS band structure as in Fig. 1. With increasing number of bands, the $\boldsymbol{k}\cdot\boldsymbol{p}$ method should approach the exact KS band structure for local potentials and for non-local potentials, the leading error due to band truncation $\propto (\boldsymbol{k}-\boldsymbol{k}_0)^2$ should vanish. However, in practice, the $\boldsymbol{k}\cdot\boldsymbol{p}$ band structures can converge slowly with number of bands and at some point, stop improving due to numerical inaccuracies in the matrix elements. To obtain an accurate interpolated band structure in the entire Brillouin zone, extrapolating from multiple $\boldsymbol{k}_n$ points can thus be an attractive option. Moreover, in typical DFT calculations of solids, the KS wave functions are available for a finite number of $\boldsymbol{k}$ points, as needed to converge the electronic density. In extrapolating from multiple $\boldsymbol{k}$ points, however, discontinuities arise at the meeting points of two extrapolations. Extrapolating from $\boldsymbol{k}_0$ and $\boldsymbol{k}_1$, we would in general find that $\varepsilon^{\boldsymbol{k}\cdot\boldsymbol{p}}_{\boldsymbol{k}_0}(\boldsymbol{k}) \neq \varepsilon^{\boldsymbol{k}\cdot\boldsymbol{p}}_{\boldsymbol{k}_1}(\boldsymbol{k})$, where the subscript denotes the wave vector used to construct the $\boldsymbol{k}\cdot\boldsymbol{p}$ Hamiltonian. One option is simply to average between different $\boldsymbol{k}\cdot\boldsymbol{p}$ results; to exemplify, $\overline{\varepsilon^{\boldsymbol{k}\cdot\boldsymbol{p}}}(\boldsymbol{k}) = a\varepsilon^{\boldsymbol{k}\cdot\boldsymbol{p}}_{\boldsymbol{k}_0}(\boldsymbol{k}) + (1-a)\varepsilon^{\boldsymbol{k}\cdot\boldsymbol{p}}_{\boldsymbol{k}_1}(\boldsymbol{k})$. However, as the errors arising in two extrapolations often share sign, wiggles, and spurious band extrema can arise.

In the $\boldsymbol{k}\cdot\tilde{\boldsymbol{p}}$ method, a correction term is introduced that ensures that the $\boldsymbol{k}\cdot\boldsymbol{p}$ energies generated by extrapolating from, for instance, $\boldsymbol{k}_0$ matches the neighbouring $\boldsymbol{k}$ points in the coarse KS mesh, i.e. $\varepsilon^{\boldsymbol{k}\cdot\tilde{\boldsymbol{p}}}_{\boldsymbol{k}_0}(\boldsymbol{k}_1) = \varepsilon^{\mathrm{KS}}(\boldsymbol{k}_1)$. This correction term is akin to Kane parameters in few-band $\boldsymbol{k}\cdot\boldsymbol{p}$ models,[53,54] accounting for bands not included explicitly in the $\boldsymbol{k}\cdot\boldsymbol{p}$ Hamiltonian. In a three-dimensional reciprocal space, for the case of $\boldsymbol{k}$ values enclosed by a tetrahedron with corners at $\boldsymbol{k}_0$ (reference point), $\boldsymbol{k}_1$, $\boldsymbol{k}_2$, and $\boldsymbol{k}_3$ (target points), the correction term takes the form:

$$\Delta H(\boldsymbol{k}) = \frac{m}{\hbar}\sum_{n=1,2,3}\Omega_n(\boldsymbol{k})\frac{(\boldsymbol{k}-\boldsymbol{k}_0)^2}{(\boldsymbol{k}_n-\boldsymbol{k}_0)^2}\sum_i \delta\varepsilon_{i,\boldsymbol{k}_n} V_{i,\boldsymbol{k}_n} V^{\dagger}_{i,\boldsymbol{k}_n}\,. \tag{2}$$

Here $\delta\varepsilon_{i,\boldsymbol{k}_n} = \varepsilon^{\mathrm{KS}}_i(\boldsymbol{k}_n) - \varepsilon^{\mathrm{k\cdot p}}_{i,\boldsymbol{k}_0}(\boldsymbol{k}_n)$ and $V_{i,\boldsymbol{k}_n}$ are the eigenvectors of Eq. (1) for $\boldsymbol{k}$ values at the respective target points $n = 1, 2, 3$. $V_{i,\boldsymbol{k}_n} V^{\dagger}_{i,\boldsymbol{k}_n}$ are band projections which account for band crossings and changing band nature, whereas $\Omega_n(\boldsymbol{k})$ is an angular projection term, given by

$$\Omega_n(\boldsymbol{k}) = \frac{\left[\boldsymbol{s}_n\cdot(\boldsymbol{k}-\boldsymbol{k}_0)\right]^2}{\sum_n\left[\boldsymbol{s}_n\cdot(\boldsymbol{k}-\boldsymbol{k}_0)\right]^2}\,, \tag{3}$$

with $\boldsymbol{s}_1 = (\delta\boldsymbol{k}_2\times\delta\boldsymbol{k}_3)\,/\,[\delta\boldsymbol{k}_1\cdot(\delta\boldsymbol{k}_2\times\delta\boldsymbol{k}_3)]$ where $\delta\boldsymbol{k}_i = \boldsymbol{k}_i - \boldsymbol{k}_0$ and similarly for $\boldsymbol{s}_2$ and $\boldsymbol{s}_3$. For sake of symmetry, since several of $\boldsymbol{k}\cdot\tilde{\boldsymbol{p}}$ extrapolations starting from the coarse mesh ends up at same dense mesh points, the method averages over different $\boldsymbol{k}\cdot\tilde{\boldsymbol{p}}$ results, which smoothen results slightly.[33]

C. Boltzmann transport equation

The Boltzmann transport equation (BTE) in the relaxation-time approximation is commonly used to study the electronic transport in solids. In this approach, the conductivity σ and Seebeck coefficient S, can be expressed in terms of the transport-spectral function $\Sigma(\varepsilon)$, as follows (tensor indices suppressed),

$$\sigma = e^2\int_{-\infty}^{\infty}\mathrm{d}\varepsilon\left(-\frac{\partial f_{\mathrm{FD}}(\varepsilon)}{\partial\varepsilon}\right)\Sigma(\varepsilon)\,, \tag{4}$$

$$T\sigma S = e\int_{-\infty}^{\infty}\mathrm{d}\varepsilon\left(-\frac{\partial f_{\mathrm{FD}}(\varepsilon)}{\partial\varepsilon}\right)\Sigma(\varepsilon)(\varepsilon-\mu_{\mathrm{F}})\,. \tag{5}$$

Here, the Fermi window $\left(-\frac{\partial f_{\mathrm{FD}}(\varepsilon)}{\partial\varepsilon}\right)$ is given by the derivative of the Fermi-Dirac distribution function. The transport spectral function is given by

$$\Sigma(\epsilon) = \frac{1}{VN}\sum_{\boldsymbol{k},i} v_i(\boldsymbol{k})v_i(\boldsymbol{k})\tau_i(\boldsymbol{k})\,\delta\left(\varepsilon-\varepsilon_i(\boldsymbol{k})\right)\,, \tag{6}$$

where $v_i(\boldsymbol{k})$ are the group velocities. In our study, $\Sigma(\varepsilon)$ was computed with BoltzTrap[8] based on $\boldsymbol{k}\cdot\tilde{\boldsymbol{p}}$ interpolated band structures. As the purpose of our study was to probe the effect of the band structure account, we simply employed the constant-relaxation time approximation $\tau_i(\boldsymbol{k}) = \tau$.

D. Convergence study

Our $\boldsymbol{k}$-mesh convergence study for the Seebeck coefficient of GaAs is shown in Fig. 2 with n- and p- carrier densities set to $10^{18}\,\mathrm{cm}^{-3}$ (upper and lower panel, respectively), whereas Fig. 3 shows the corresponding convergence study for the conductivity in the p-doped case. The thin orange, blue dashed, and thick gray curves are generated with respectively $6\times6\times6$, $12\times12\times12$, and $48\times48\times48$ $\boldsymbol{k}$-meshes. The green dashed-dotted and black curves with short dashes are based on the KS solutions of a $6\times6\times6$ and $12\times12\times12$ mesh, both interpolated using the $\boldsymbol{k}\cdot\tilde{\boldsymbol{p}}$ method to a $48\times48\times48$ mesh. At 200 K, the

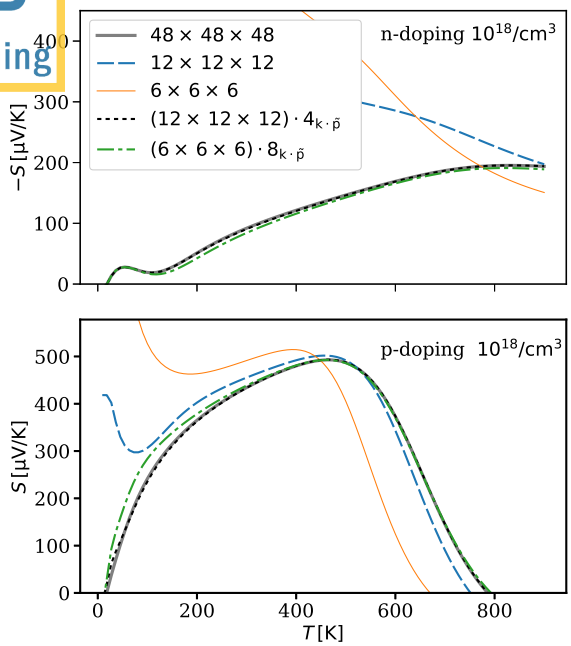

FIG. 2: Seebeck coefficient of GaAs as function of temperature calculated for different $\boldsymbol{k}$-meshes, comparing standard and $\boldsymbol{k}\cdot\tilde{\boldsymbol{p}}$ based results. The upper (lower) panel shows results for n-(p)doping of 10^{18} cm^{-3}. Here $(12\times12\times12)_{4_{\boldsymbol{k}\cdot\tilde{\boldsymbol{p}}}}$ denotes that the $12\times12\times12$ mesh was interpolated to a $48\times48\times48$ mesh.

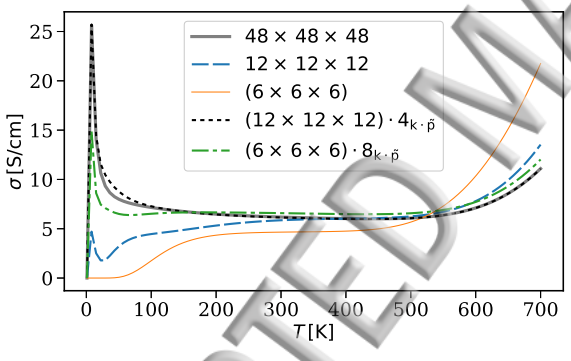

FIG. 3: Conductivity of GaAs with p-doping as in Fig. 2.

interpolated Seebeck coefficient based on a $12\times12\times12$ mesh deviates from the reference $48\times48\times48$ KS result by no more than 1.4% for n and 0.65% for p doping. The deviation is generally slightly larger at lower temperatures and smaller at higher temperatures. Interpolating from a $6\times6\times6$ mesh, the deviations increase to 17% (3.6%) for n (p) doping, which is too inaccurate in a quantitative analysis, but deviations are modest at high temperatures. Fig. 2 shows that the interpolation from a $12\times12\times12$, but not from $6\times6\times6$ mesh, is able to resolve the spike in the conductivity at 8 K, with a peak value differing by no more than 0.08S/cm from the reference KS results. This result can be linked to how well the interpolation is

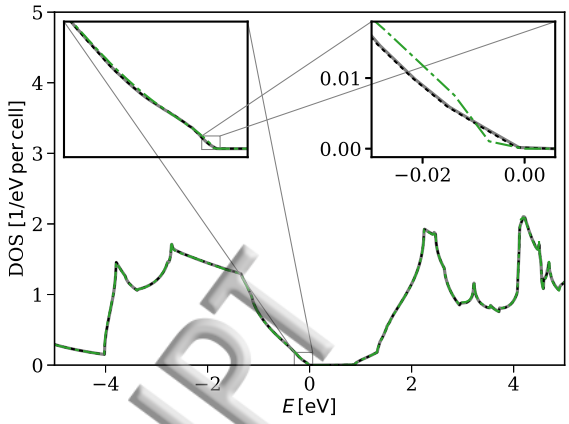

FIG. 4: Density of states of GaAs generated with the tetrahedron method using a $48\times48\times48$ mesh based on standard KS results (full grey curve) and $\boldsymbol{k}\cdot\tilde{\boldsymbol{p}}$ interpolation from a $12\times12\times12$ mesh (dashed black) and a $6\times6\times6$ mesh (dash-dotted green). The insets each scale the figure by a factor of 10.

able to able to resolve the density of states very close to the conduction band edge, as shown in Fig. 4. At this low temperature, the transport is completely dominated by holes close to the band edge. The figure shows that while interpolating from a $6\times6\times6$ is sufficient to resolve the overall DOS, interpolating from $12\times12\times12$ mesh is needed to recover the DOS with high precision close to the band edge.

While accuracy can be enhanced by increasing the number of empty bands, we found that interpolating a $12\times12\times12$ $\boldsymbol{k}$-mesh using a convenient number of bands, at least twice that of the number of occupied bands, generally gives a highly accurate interpolation of the near-gap conduction and valence band states contributing to the thermoelectric transport. The $\boldsymbol{k}\cdot\tilde{\boldsymbol{p}}$ method can be extended to very dense grids at low computational cost. The results in the next section are based on an interpolation to a $60\times60\times60$ mesh for GaAs and InP and to a $96\times96\times96$ mesh for PbTe.

III. RESULTS

A. GaAs and InP: n-doping

While bulk GaAs and InP are poor thermoelectric materials, nanowires of these compounds could serve as highly efficient thermoelectric devices.[56,57] The transport properties of GaAs and InP are also of interest in high-frequency electronics, light emission and detection, and photovoltaics. Owing to their high material quality and dopability, they are well suited as test systems for exploring how using different XC functional affects thermoelectric transport properties.

A Pisarenko plot comparing the experimental[58,59] and

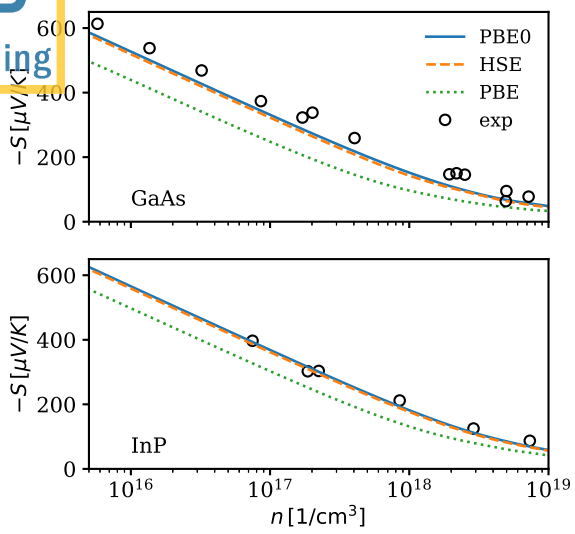

FIG. 5: Pisarenko plot of the Seebeck coefficient of n-doped GaAs and InP at 300 K comparing theory and experiment. Experimental data for GaAs as given by Pichanusakorn[58] and references therein, and for InP by Kesamanly et al.[59] as reported by Rode.[58]

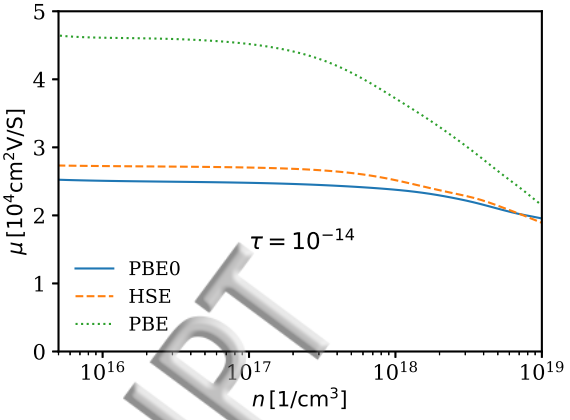

FIG. 6: Mobility of GaAs calculated with a constant relaxation time $\tau = 10^{-14}$s.

calculated Seebeck coefficients of n-doped GaAs and InP at 300 K is shown in Fig. 5. For all doping concentration, the two hybrids HSE and PBE0 give similar results, which agree better with experiments than PBE. The better agreement for the two hybrids can be linked to more accurate band gaps resulting in a more accurate band curvature close to the conduction band minimum, as shown in table I. The calculated effective masses were here estimated with the standard $\boldsymbol{k}\cdot\boldsymbol{p}$ method with a small, rather than infinitesimal, $|\delta\boldsymbol{k}|$ of 0.01/Å, as spin-orbit coupling distorts the band structure close to the Γ point.

TABLE I: Band gap and effective mass of GaAs and InP.

	GaAs	InP
Method	Δ_Γ[eV] (m_c)	Δ_Γ[eV] (m_c)
PBE	0.38 (0.028)	0.50 (0.043)
HSE	1.13 (0.063)	1.23 (0.074)
PBE0	1.64 (0.063)	1.75 (0.081)
Exp.[a]	1.519 (0.067)	1.4236 (0.0795)

[a]Experimental band gap energies and effective masses are based on the recommended values of Vurgaftman et al.[44].

In the non-degenerate limit of a n-doped single parabolic band model at constant scattering time, the Seebeck coefficient can be expressed as follows,[60]

$$S = -\frac{k_B}{e}\left[\frac{5}{2} - \log\left(\frac{n/2}{(2\pi m_e k_B T)^{3/2}}\right)\right]. \qquad (7)$$

The logarithmic dependence on the carrier density explains why the three methods give similar, virtually linear, slopes up to about $10^{18}\,cm^{-3}$ in Fig. 5. In this formula, using two different masses m_1 and m_2 results in constant shift in the Seebeck coefficient, as follows

$$S_{m_1} - S_{m_2} = \frac{3}{2}\log(\frac{m_2}{m_1}). \qquad (8)$$

This shift agrees fairly well with the difference in offset in Fig. 2. To exemplify, at a doping concentration of $5\cdot10^{15}\,cm^{-3}$, the Seebeck coefficient of PBE is shifted 100 μV/K compared to HSE, while Eq. (8) gives 105 μV/K with effective masses provided in table I. At higher doping concentrations, the Seebeck coefficients become more similar, which is related both to non-parabolicity and the fact the electrons become degenerate.

Figure 6 shows that the choice of XC functional also has a strong effect on the mobility $\mu = \sigma/en$ at a constant relaxation time. That the mobility is 1.7 larger for PBE than HSE at a doping concentration of $5\cdot10^{15}\,cm^{-3}$ is similar to, but somewhat smaller than $m_{PBE}/m_{HSE} = 2.3$. The larger change in mobility with doping concentration for PBE than HSE and PBE0 can be linked to the increased non-parabolicity at smaller bandgaps. In some studies, the relaxation time is fitted to the measured mobility at a given temperature and doping concentration. This fitting can veil the role of the XC functional at a given temperature and doping concentration, but this would not mimic the effect of non-parabolicity at higher temperatures or doping concentrations. As we employed a constant relaxation time, none of the methods are even close to describing measured drops in mobility (not shown in figure), which is about a factor of five from $5\cdot10^{15}\,cm^{-3}$ to $10^{19}\,cm^{-3}$.[61] The large drop can be linked to impurity scattering arising from dopants, which in turn could also explain the underestimated Seebeck coefficient even when employing hybrid functionals.[58]

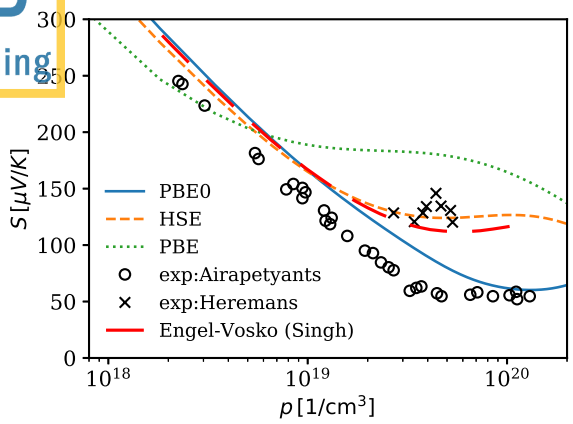

FIG. 7: The Seebeck coefficient of PbTe as a function of p-carrier concentration at 300 K. Circles represent experimental data of Airapetyants et al.,[68] while crosses correspond to Heremans et al.[35]

B. PbTe

PbTe has been used in radioisotope thermoelectric generators, powering, for instance, the Viking space probes.[62] Even if it was one of the first thermoelectric materials discovered, PbTe and related chalcogenides have continued to attract scientific interest, with new record ZTs being reported the last decade.[35,37,63–65] In 2008 Heremans et al.[35] measured a ZT of 1.5 at 773 K, which was achieved through 2% Tl substitution of the Pb site. The high efficiency has been attributed to the formation of resonant states in the valence band.[35,63–65] Using the Engel-Vosko (EV) GGA functional,[66] which avoids the severe band gap underestimation of standard GGAs, Singh[67] calculated the Seebeck coefficient of PbTe. However, even if doping was only accounted for implicitly by shifting the Fermi level, beyond a p-carrier concentration of $10^{19}\,\mathrm{cm}^{-3}$, the results agreed better with the high Seebeck coefficient measured by Heremans. et al. than with the lower Seebeck coefficient reported by Airapetyants et al.,[68] and others for several different dopants.[65] This finding motivated us to re-examine the Seebeck coefficient using hybrid functionals.

Figure 7 compares the Seebeck calculated based on PBE, HSE, and PBE0 with the experimental measurements of Airapetyants e. al.[68] and Heremans et al.,[35] as presented by Pei. et al.[65] For carrier concentrations less than about $5\cdot10^{18}\,\mathrm{cm}^{-3}$, both hybrids give similar results and slightly overestimate the experimental Seebeck coefficient. While the magnitude agrees with experiment, the slope of the Seebeck coefficient with PBE becomes inaccurate beyond $2\cdot10^{18}\,\mathrm{cm}^{-3}$. At low doping concentrations, the difference between PBE and the hybrids can be linked to the band curvature of the L point valence-band maximum, which in turn is related to the band gap. The PBE band gap is 0.065 eV, wheres that of HSE is 0.42 eV and that of PBE0 is 0.96 eV. As the experimental band gap is 0.2 eV at 0 K and 0.3 eV at room temperature,[69] PBE severely underestimates the gap, but PBE0 considerably overestimates it. At a doping concentration of about $5\cdot10^{19}\,\mathrm{cm}^{-3}$, PBE overestimates the Seebeck coefficient by close to a factor of four, whereas HSE agrees well with EV calculations of Singh,[67] and the measurements of Heremans et al.[35] PBE0, on the other hand, agrees well with the results of Airapetyants et al.,[68] and is therefore in line with earlier investigations attributing the high Seebeck coefficient of Heremans et al. to the effect of Tl impurities.[35,63–65]

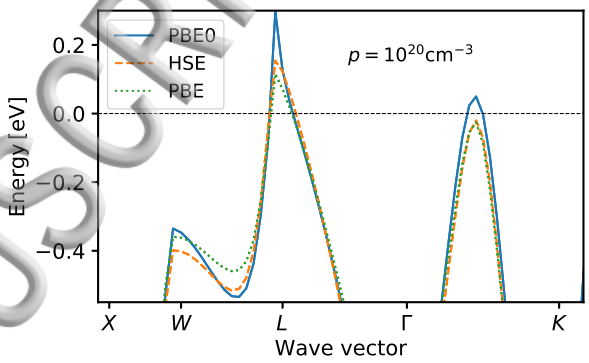

FIG. 8: Band structure of PbTe. The Fermi level is set to a p-carrier concentration of $2\cdot10^{19}\,\mathrm{cm}^{-3}$

The valence band structure of PbTe calculated with the three different methods, as shown in Fig. 8, casts some light on the difference between HSE and PBE0 at higher doping concentration. The Fermi level was set to yield a p-carrier concentration of $10^{20}\,\mathrm{cm}^{-3}$ for each of the three XC functionals, as the Seebeck coefficients of the XC functionals differ strongly in this region. A noticeable feature of the PbTe band structure is its approximate valley convergence of the valence band, i.e. the energetic alignment of the band maximum at the L point and the maximum along the Σ line between Γ and K. While the Σ valley of HSE is non-degenerate at this doping concentration, it becomes degenerate with PBE0. The L valley of PBE0 is also narrower than that of HSE. Both these features contribute to reducing the Seebeck coefficient of PBE0 compared to HSE, but they also enhance the conductivity, which we found to be 1.4 times larger for PBE0 than HSE at this doping concentration.

Finally, Fig 9 compares the calculated Seebeck coefficient of n-doped PbTe with experimental data by Pei. et al.[70] Similar to the case of GaAs, both hybrids give similar results and significantly improves the agreement with experiment, but the calculated Seebeck coefficient is lower than the measured.

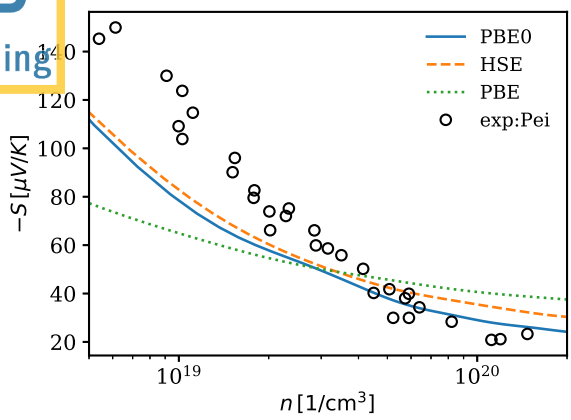

FIG. 9: Seebeck coefficient of PbTe as a function of n-carrier concentration at 300 K. The circles represent the experimental data of Pei et al.[70]

IV. OUTLOOK

First-principles methods, such as DFT, regularly provide highly accurate predictions for a range of material properties, including structural, energetic, and optical properties. However, for electronic transport in thermoelectric materials, DFT-based studies are generally limited to qualitative analysis or material screening. In this paper, we have shown that the direct band gap underestimation of standard GGAs is one source of inaccuracy in such calculations, as the band gap is strongly linked to the band curvature of conduction and valence bands. However, even if we can expect hybrid functionals to improve the accuracy, in particular for the Seebeck coefficient, other effects must also be accounted for to realize truly predictive thermoelectric transport calculations. Scattering mechanisms should also be described based on first-principles calculations and the effect of thermal expansion and explicit doping on the band structure should be included.

Even in screening studies, when a quantitative comparison between theory and experiments is not sought, our study illustrates pitfalls of using standard GGA. Some materials might be deemed more favorable than others due to inaccurate effective masses caused by band gap underestimation. Moreover, valley convergence, one of the most promising ways of optimizing electronic transport properties, can be fortuitous and arise due to computational choices. We have shown that even if the hybrids HSE and PBE0 provide more accurate band structures than GGAs, the hybrids provide somewhat differing accounts of the valley convergence, which in turn affects the Seebeck coefficient. We also note that while hybrid functionals generally improve the description of electron quasiparticle band gaps compared to GGAs, their ability to accurately describe the full band structure in the near gap region, and thus transport spectral function $\Sigma(\epsilon)$, has not been widely assessed.

Finally, we have shown that by improving the recent $\boldsymbol{k}\cdot\tilde{\boldsymbol{p}}$ method, we can accurately interpolate the band structure and thus overcome the $\boldsymbol{k}$-point sampling issue of hybrid functional based transport calculations. Our study should motivate using wave-function based interpolation methods in combination with more advanced first-principles methods in future screening studies or as input in machine learning, of thermoelectric material properties.

V. ACKNOWLEDGEMENT

We thank Ole Martin Løvvik and Espen Flage-Larssen for discussions. Computations were performed on the Abel and Stallo high performance cluster through a NOTUR allocation. This work is part of THELMA project (Project No. 228854) supported by the Research Council of Norway.

* Electronic address: kristian.berland@smn.uio.no

[1] X. Zhang and L.-D. Zhao, J. Materiomics **1**, 92 (2015).
[2] J. Carrete, N. Mingo, S. Wang, and S. Curtarolo, Adv. Funct. Mater. **24**, 7427 (2014).
[3] L. Xi, J. Yang, L. Wu, J. Yang, and W. Zhang, J. Materiomics **2**, 114 (2016).
[4] J. Zhang, L. Song, G. K. Madsen, K. F. Fischer, W. Zhang, X. Shi, and B. B. Iversen, Nat. Commun. **7** (2016).
[5] W. Chen, J.-H. Pohls, G. Hautier, D. Broberg, S. Bajaj, U. Aydemir, Z. M. Gibbs, H. Zhu, M. Asta, G. J. Snyder, et al., J. Mater. Chem. C **4**, 4414 (2016).
[6] G. K. H. Madsen, J. Am. Chem. Soc. **128**, 12140 (2006).
[7] F. Ricci, W. Chen, U. Aydemir, G. J. Snyder, G.-M. Rignanese, A. Jain, and G. Hautier, Sci. Data **4**, 170085 (2017).
[8] G. K. H. Madsen and D. J. Singh, Comput. Phys. Commun. **175**, 67 (2006).
[9] J. P. Perdew, K. Burke, and M. Ernzerhof, Phys. Rev. Lett. **77**, 3865 (1996).
[10] J. P. Perdew, M. Ernzerhof, and K. Burke, J. Chem. Phys. **105**, 9982 (1996).
[11] J. Heyd, G. E. Scuseria, and M. Ernzerhof, J. Chem. Phys. **118**, 8207 (2003).
[12] G. Onida, L. Reining, and A. Rubio, Rev. Mod. Phys. **74**, 601 (2002).
[13] F. Aryasetiawan and O. Gunnarsson, Rep. Prog. Phys. **61**, 237 (1998).
[14] J. O. Sofo and G. D. Mahan, Phys. Rev. B **49**, 4565 (1994).
[15] Y. Pei, H. Wang, and G. J. Snyder, Adv. Mater. **24**, 6125 (2012).
[16] K. Berland, X. Song, P. A. Carvalho, C. Persson, T. G. Finstad, and O. M. Løvvik, J. App. Phys. **119** (2016).

[17] X. Chen, D. Parker, M.-H. Du, and D. J. Singh, New J. Phys. **15**, 043029 (2013).
[18] C. Persson, R. Ahuja, and B. Johansson, Phys. Rev. B **64**, 033201 (2001).
[19] C. Persson and S. Mirbt, Braz. J. Phys. **36**, 286 (2006).
[20] Z. H. Levine and D. C. Allan, Phys. Rev. Lett. **63**, 1719 (1989).
[21] R. Del Sole and R. Girlanda, Phys. Rev. B **48**, 11789 (1993).
[22] R. Armiento and S. Kümmel, Phys. Rev. Lett. **111**, 036402 (2013).
[23] E. Engel and S. H. Vosko, Phys. Rev. B **47**, 13164 (1993).
[24] F. Tran and P. Blaha, Phys. Rev. Lett. **102**, 226401 (2009).
[25] O. Gritsenko, R. van Leeuwen, E. van Lenthe, and E. J. Baerends, Phys. Rev. A **51**, 1944 (1995).
[26] M. Kuisma, J. Ojanen, J. Enkovaara, and T. T. Rantala, Phys. Rev. B **82**, 115106 (2010).
[27] E. L. Shirley, Phys. Rev. B **54**, 16464 (1996).
[28] D. Prendergast and S. G. Louie, Phys. Rev. B **80**, 235126 (2009).
[29] I. Souza, N. Marzari, and D. Vanderbilt, Phys. Rev. B **65**, 035109 (2001).
[30] A. A. Mostofi, J. R. Yates, G. Pizzi, Y.-S. Lee, I. Souza, D. Vanderbilt, and N. Marzari, Comput. Phys. Commun. **185**, 2309 (2014).
[31] N. Marzari, A. A. Mostofi, J. R. Yates, I. Souza, and D. Vanderbilt, Rev. Mod. Phys. **84**, 1419 (2012).
[32] G. Pizzi, D. Volja, B. Kozinsky, M. Fornari, and N. Marzari, Comput. Phys. Commun. **185**, 422 (2014).
[33] K. Berland and C. Persson, Comp. Mater. Sci. **134**, 17 (2017).
[34] C. Persson and C. Ambrosch-Draxl, Comput. Phys. Commun. **177**, 280 (2007).
[35] J. P. Heremans, V. Jovovic, E. S. Toberer, A. Saramat, K. Kurosaki, A. Charoenphakdee, S. Yamanaka, and G. J. Snyder, Science **321**, 554 (2008).
[36] W. Liu, X. Tan, K. Yin, H. Liu, X. Tang, J. Shi, Q. Zhang, and C. Uher, Phys. Rev. Lett. **108**, 166601 (2012).
[37] Y. Pei, X. Shi, A. LaLonde, H. Wang, L. Chen, and G. J. Snyder, Nature **473**, 66 (2011).
[38] G. Kresse and J. Hafner, Phys. Rev. B **47**, 558 (1993).
[39] G. Kresse and J. Furthmller, Comput. Mat. Sci. **6**, 15 (1996).
[40] G. Kresse and J. Furthmüller, Phys. Rev. B **54**, 11169 (1996).
[41] M. Gajdoš, K. Hummer, G. Kresse, J. Furthmüller, and F. Bechstedt, Phys. Rev. B **73**, 045112 (2006).
[42] J. P. Perdew, A. Ruzsinszky, G. I. Csonka, O. A. Vydrov, G. E. Scuseria, L. A. Constantin, X. Zhou, and K. Burke, Phys. Rev. Lett. **100**, 136406 (2008).
[43] P. Haas, F. Tran, and P. Blaha, Phys. Rev. B **79**, 085104 (2009).
[44] I. Vurgaftman, J. R. Meyer, and L. R. Ram-Mohan, J. App. Phys. **89**, 5815 (2001).
[45] E. Kane, J. Phys. Chem. Solids **1**, 82 (1956).
[46] J. M. Luttinger and W. Kohn, Phys. Rev. **97**, 869 (1955).
[47] M. Dresselhaus, G. Dresselhaus, and A. Jorio, *Group Theory: Application to the Physics of Condensed Matter*, SpringerLink: Springer e-Books (Springer, Berlin, Heidelberg, 2007).
[48] J. Kim, L.-W. Wang, and A. Zunger, Phys. Rev. B **57**, R9408 (1998).
[49] P. von Allmen, Phys. Rev. B **46**, 15382 (1992).
[50] S. Tomić and N. Vukmirović, J. App. Phys. **110** (2011).
[51] G. Dresselhaus, A. F. Kip, and C. Kittel, Phys. Rev. **98**, 368 (1955).
[52] M. Cardona and F. H. Pollak, Phys. Rev. **142**, 530 (1966).
[53] C. Galeriu, PhD disertation, Worcester Polytechnic Institute, Worcester (2005).
[54] L. Voon and M. Willatzen, *The k·p Method: Electronic Properties of Semiconductors* (Springer, Berlin, Heidelberg, 2009).
[55] C. J. Pickard and M. C. Payne, Phys. Rev. B **62**, 4383 (2000).
[56] M. F. ODwyer, T. E. Humphrey, and H. Linke, Nanotechnology **17**, S338 (2006).
[57] X. Zou, X. Chen, H. Huang, Y. Xu, and W. Duan, Nanoscale **7**, 8776 (2015).
[58] P. Pichanusakorn, Y. J. Kuang, C. J. Patel, C. W. Tu, and P. R. Bandaru, App. Phys. Lett. **99**, 072114 (2011).
[59] F. P. Kesamanly, D. N. Nasledov, A. Y. Nashelskii, and V. A. Skripkin, Sov. Phys. Semicond. **2**, 1221 (1969).
[60] G. Nolas, J. Sharp, and J. Goldsmid, *Thermoelectrics: Basic Principles and New Materials Developments*, Springer Series in Materials Science (Springer, Berlin, Heidelberg, 2013).
[61] M. Sotoodeh, A. H. Khalid, and A. A. Rezazadeh, J. App. Phys. **87**, 2890 (2000).
[62] Z. Dughaish, Physica B: Condensed Matter **322**, 205 (2002).
[63] M.-S. Lee and S. D. Mahanti, Phys. Rev. B **85**, 165149 (2012).
[64] C. M. Jaworski, B. Wiendlocha, V. Jovovic, and J. P. Heremans, Energy Environ. Sci. **4**, 4155 (2011).
[65] Y. Pei, A. LaLonde, S. Iwanaga, and G. J. Snyder, Energy Environ. Sci. **4**, 2085 (2011).
[66] E. Engel and S. H. Vosko, Phys. Rev. B **47**, 13164 (1993).
[67] D. J. Singh, Phys. Rev. B **81**, 195217 (2010).
[68] S. Airapetyants, M. Vinogradova, I. Dubrovskaya, N. Kolomoets, and I. Rudnik, Sov. Phys. Solid State **8**, 1069 (1966).
[69] Z. M. Gibbs, H. Kim, H. Wang, R. L. White, F. Drymiotis, M. Kaviany, and G. J. Snyder, App. Phys. Lett. **103**, 262109 (2013).
[70] Y. Pei, A. D. LaLonde, H. Wang, and G. J. Snyder, Energy Environ. Sci. **5**, 7963 (2012).
[71] A. Jain, S. P. Ong, G. Hautier, W. Chen, W. D. Richards, S. Dacek, S. Cholia, D. Gunter, D. Skinner, G. Ceder, et al., APL Mater. **1** (2013).
[72] Initial structures are obtained from the MATERIALS PROJECT.[71]

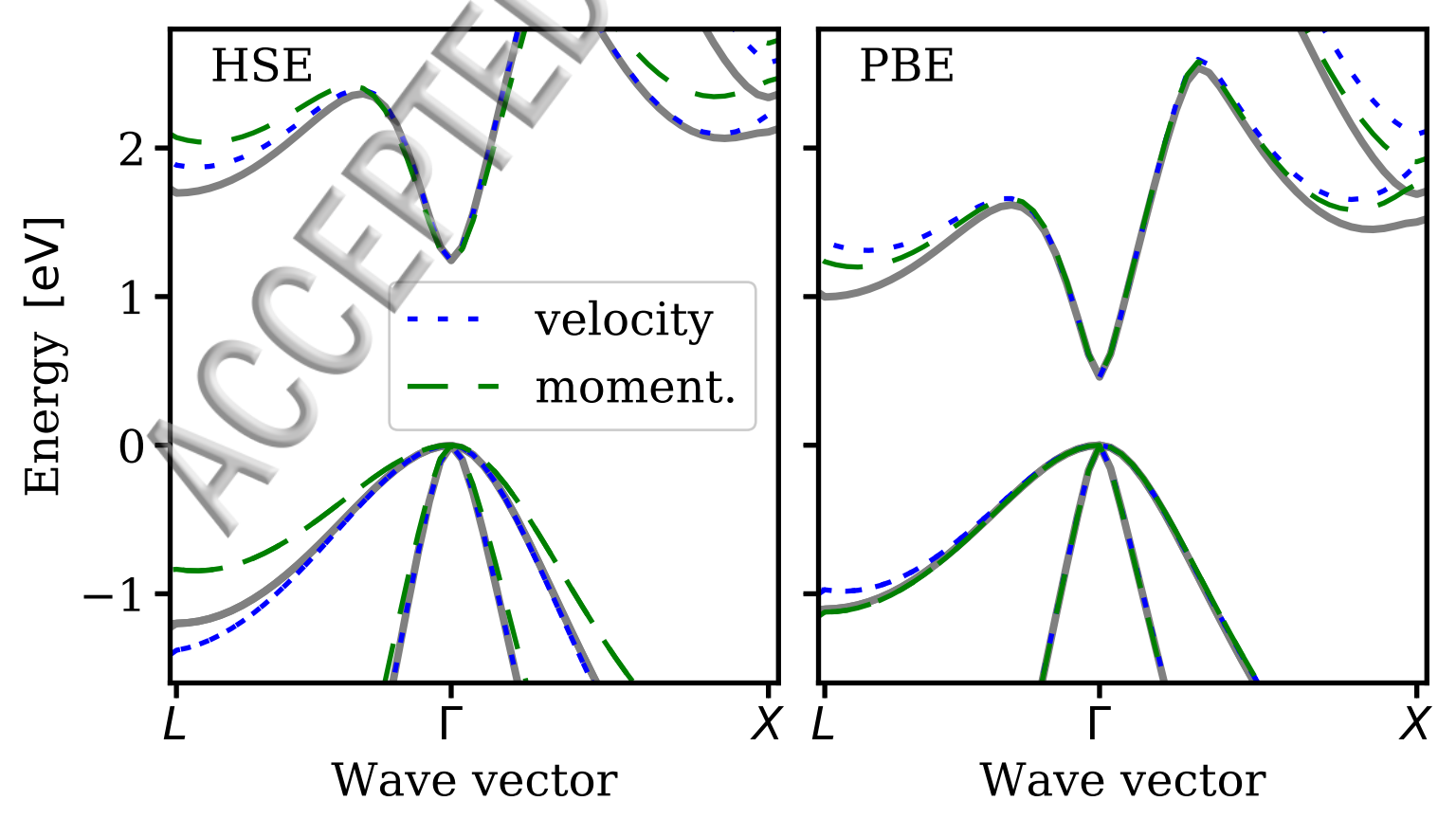
HSE
PBE
velocity
moment.
Energy [eV]
2
1
0
−1
L
Γ
X
Wave vector
ACCEPTED

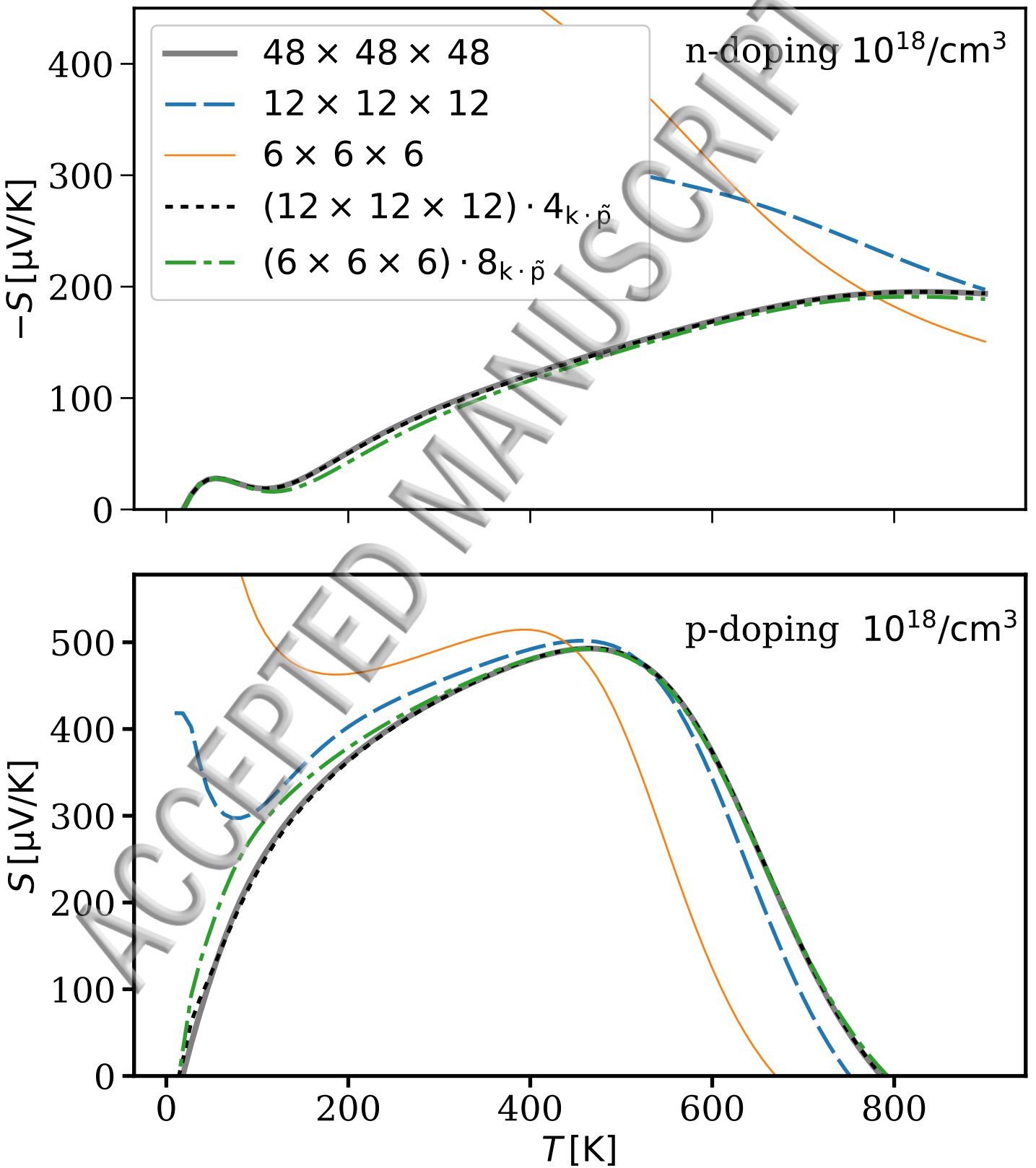

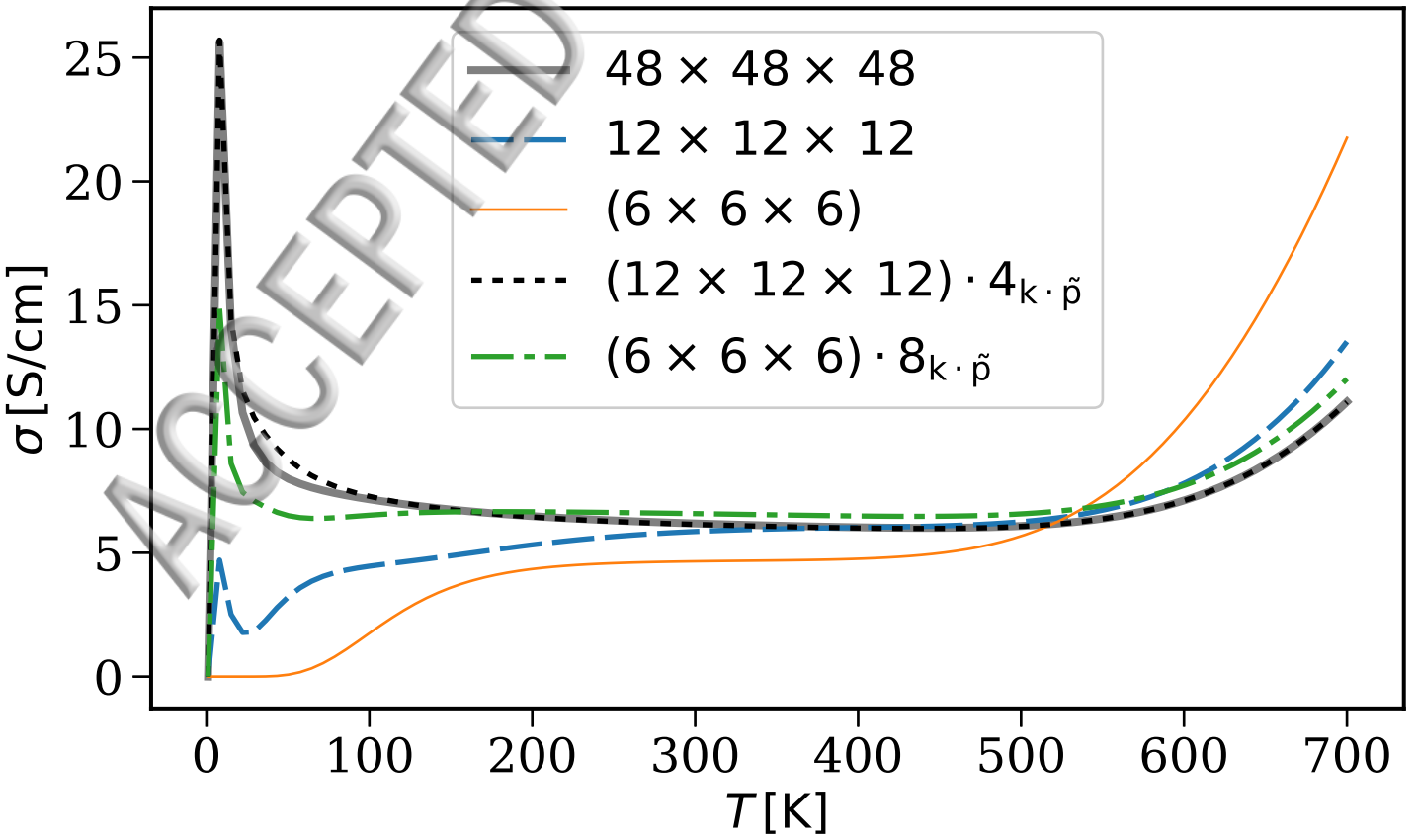
48 × 48 × 48
12 × 12 × 12
(6 × 6 × 6)
(12 × 12 × 12) · 4k · p̃
(6 × 6 × 6) · 8k · p̃
σ[S/cm]
T[K]
0
5
10
15
20
25
0
100
200
300
400
500
600
700

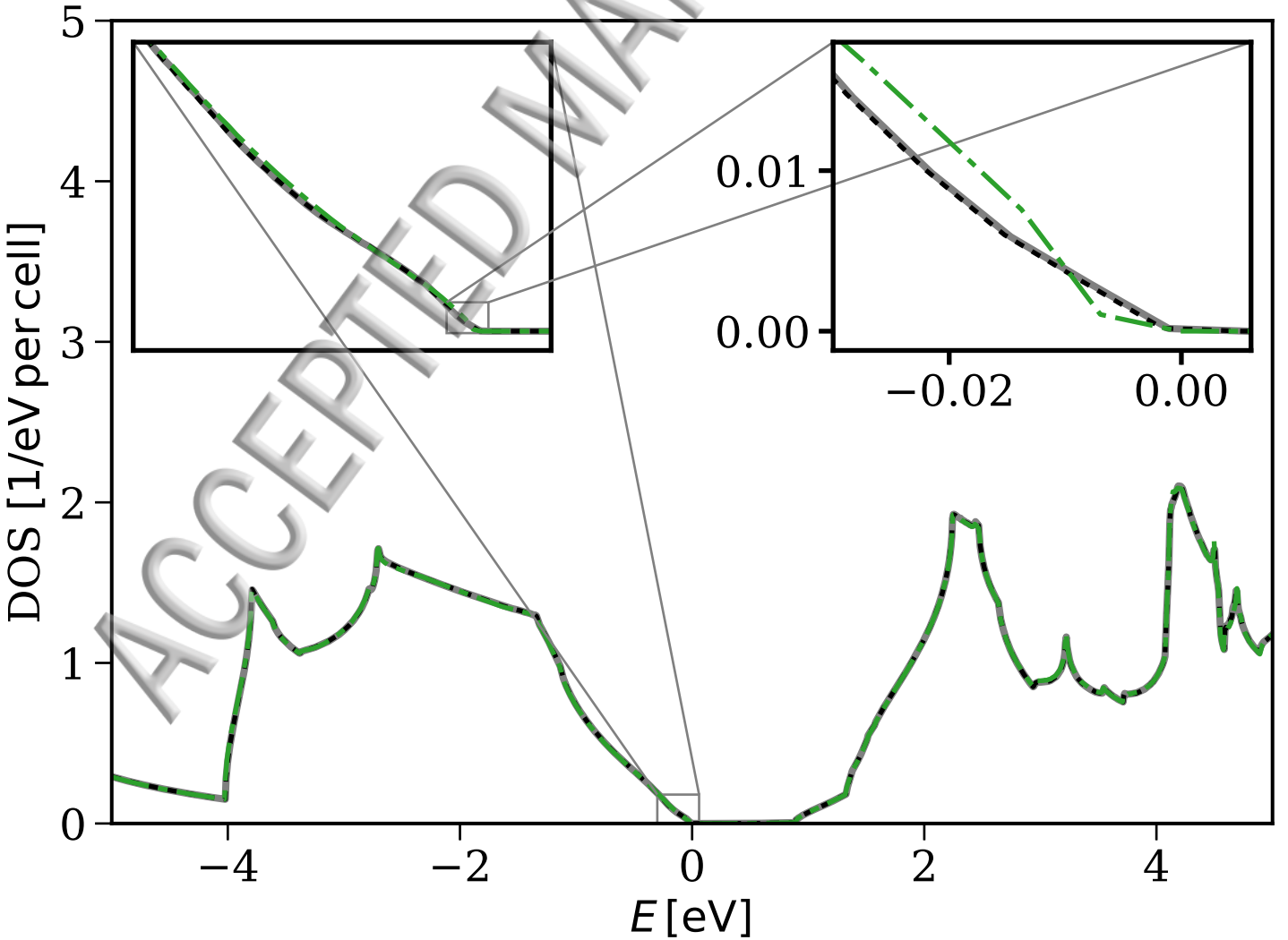

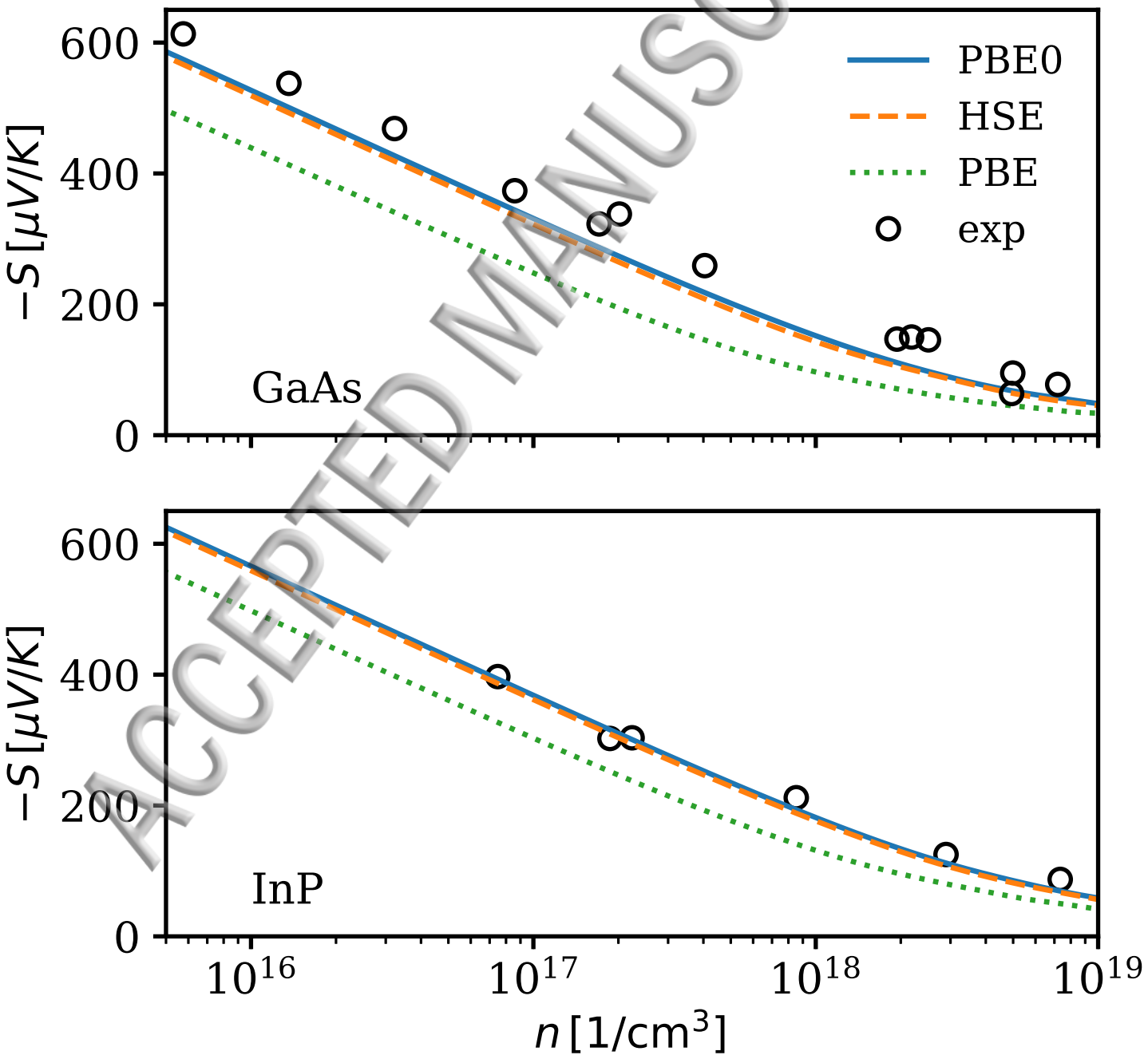

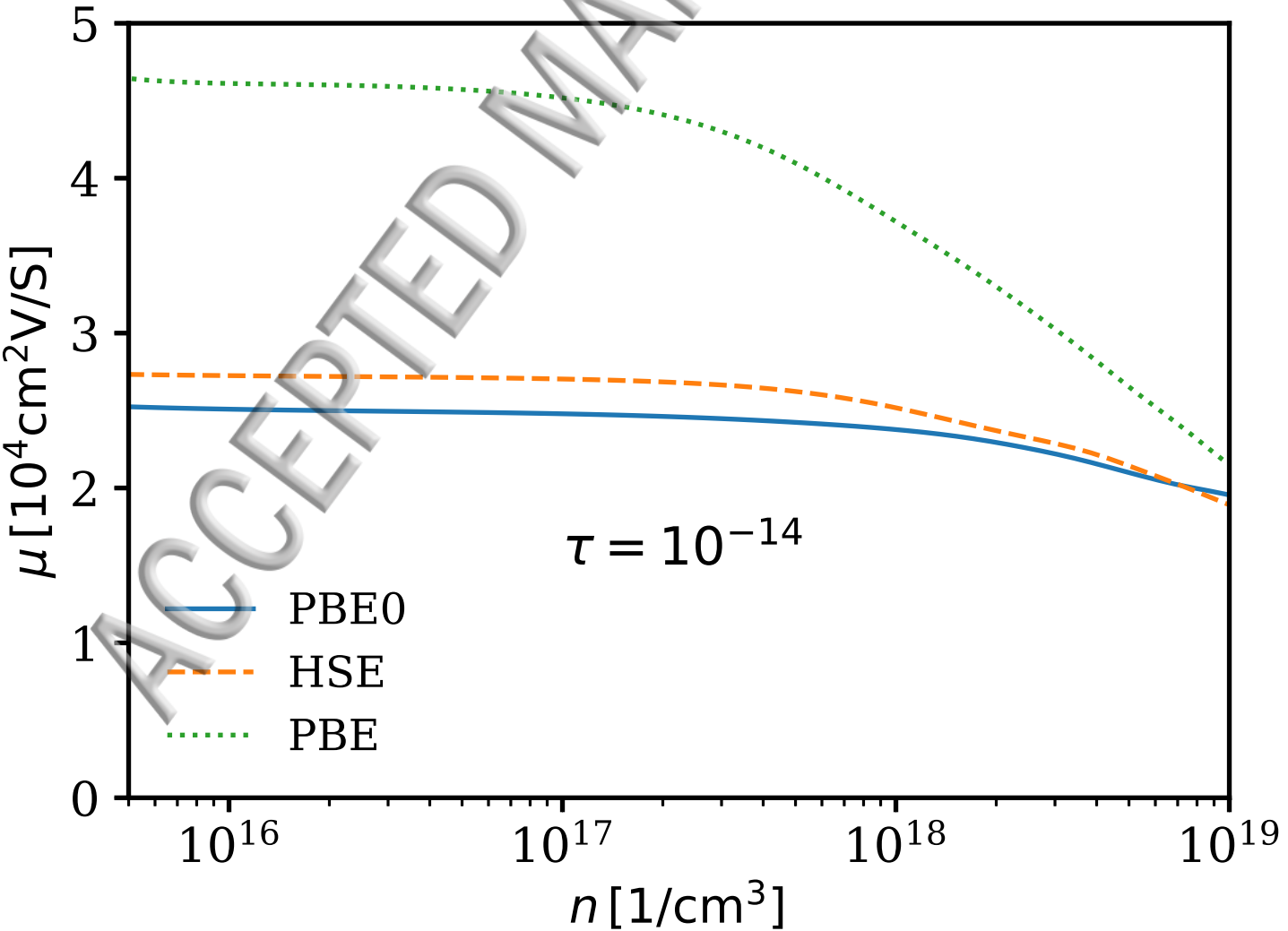

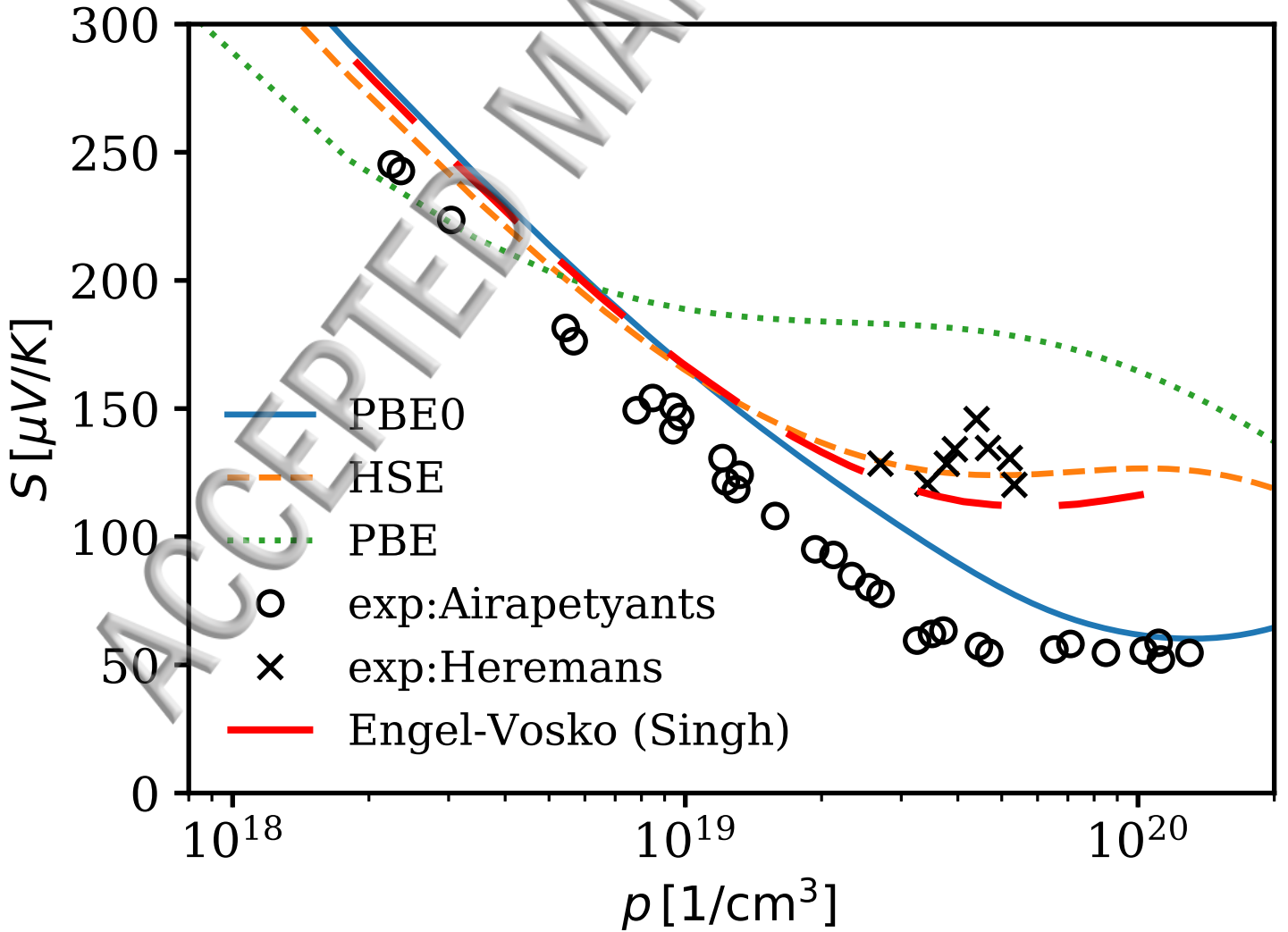

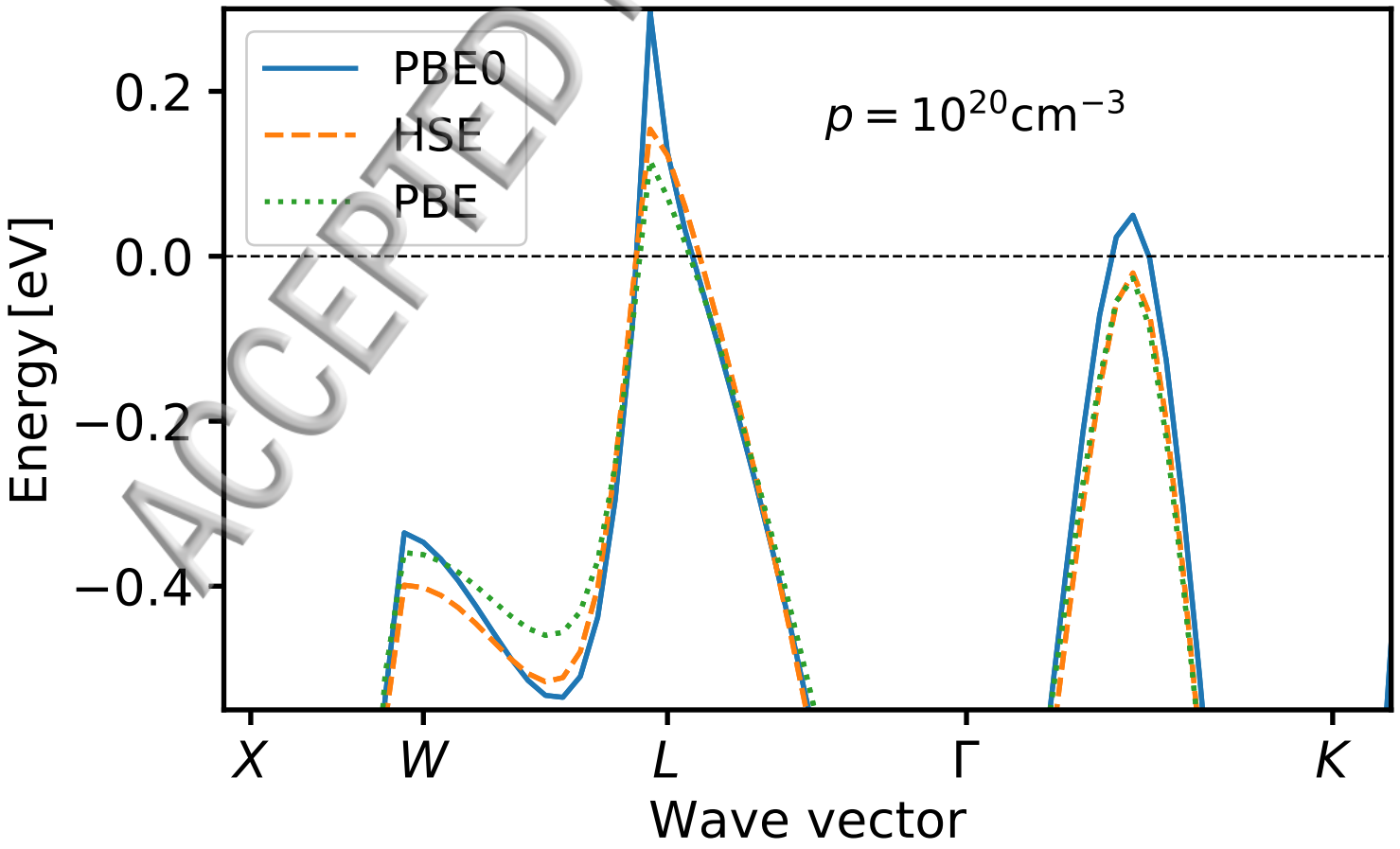
PBE0
HSE
PBE
$p = 10^{20}\mathrm{cm}^{-3}$
0.2
0.0
−0.2
−0.4
Energy [eV]
X
W
L
Γ
K
Wave vector